ISSN 1054-660X, Laser Physics, 2006, Vol. 16, No. 11, pp. 1501–1507.

Two-Mode Homodyne Tomography of Time-Encoded Single-Photon Ebits

A. Zavatta[a], M. D'Angelo[b], V. Parigi[c], and M. Bellini[a, b, *]

[a] *Istituto Nazionale di Ottica Applicata-CNR, L. go E. Fermi, 6, Florence, I-50125 Italy*

[b] *LENS, Via Nello Carrara 1, 50019 Sesto Florentino, Florence, Italy*

[c] *Department of Physics, University of Florence, Sesto Fiorentino, Florence, I-50019 Italy*

*e-mail: bellini@inoa.it

Received April 24, 2006

Abstract—We have developed a technique for dual-temporal-mode, ultrafast, time-domain, balanced homodyne detection. We have tested it by performing homodyne measurements on pairs of picosecond-duration temporal modes (or "time bins") carrying a delocalized single photon. The experimental homodyne data have been used to reconstruct both the density matrix and the two-mode Wigner function of the delocalized state, thus showing the correlations existing between the pair of temporal modes carrying the single photon.

PACS numbers: 03.67.Mn, 42.50.Dv, 03.65.Wj

DOI: 10.1134/S1054660X06110028

1. INTRODUCTION

Increasing attention has recently been given to a new quantum information perspective where the carriers of quantum information are no longer the photons but rather the field modes "carrying" them (see, e.g., [1–5] and references therein). In this context, following the road traced by Gisin's group [3–5], we have recently proposed and implemented a remotely tunable source of arbitrary time-encoded single-photon entangled states (ebits) [6]. In other words, our source produces single photons coherently delocalized in ultrashort copropagating temporal modes (or "time bins") described by the state

$$|\Psi\rangle = \alpha|1^{(n)}\rangle|0^{(n+1)}\rangle + \beta|0^{(n)}\rangle|1^{(n+1)}\rangle, \qquad (1)$$

where n and $n + 1$ denote two consecutive time bins and α and β are complex numbers such that $|\alpha|^2 + |\beta|^2 = 1$, $|1\rangle$ is a single-photon Fock state and $|0\rangle$ is the vacuum.

Single-photon ebits have been proven to enable linear optics quantum teleportation [1, 7] and play a central role in linear optics quantum computation [2, 8]. Furthermore, time-bin entanglement has been proven suitable for long-distance applications [7, 9], where the insensitivity to both depolarization and polarization fluctuations becomes a strong requirement. In addition, since the carriers of entanglement are naturally separated (i.e., no further optical element is required) and undergo the same losses, entanglement in time is less sensitive to losses and easier to purify [10].

All these applications rely on the existence of an adequate detection scheme, enabling one to analyze, in terms of both purity and correlations, the produced single-photon time-bin entangled systems. In this paper, we present the experimental characterization of our source of temporally delocalized single photons by means of a novel dual-mode homodyne technique based on the ultrafast time-domain balanced homodyne detection scheme recently developed in our lab [11, 12]. This has allowed us to perform two-mode quantum tomography on these single-photon time-bin entangled states and to reconstruct both their density matrix and two-mode Wigner function. The results are in excellent agreement with the theoretical predictions; in particular, both the two-mode Wigner function and the two-mode density matrix reproduce the coherence of the single-photon state of Eq. (1), as well as the correlations characterizing the two time bins carrying the delocalized single photon. Our results indicate the high efficiency of our detection scheme, together with its ability to resolve and analyze picosecond pulses (temporal modes) separated by just a few nanoseconds.

In Section 2, we describe the experimental setup and briefly discuss the working principle of our source for the remote preparation of single-photon time-encoded entangled states. After the description of the preparation scheme, we focus our attention on the detection scheme. In Section 3, we give an overview of some basic concepts of quantum homodyne tomography. In Section 3.2, we present the results obtained by performing single-mode balanced homodyne detection on two different systems: (1) a single-photon Fock state and (2) a temporally delocalized single photon of the kind of Eq. (1). The results of the first measurement allow us to evaluate the efficiency of our detection scheme; the second set of data, instead, simply represent a reference point for better appreciating the importance of performing two-mode homodyne tomography. In Section 3.3,

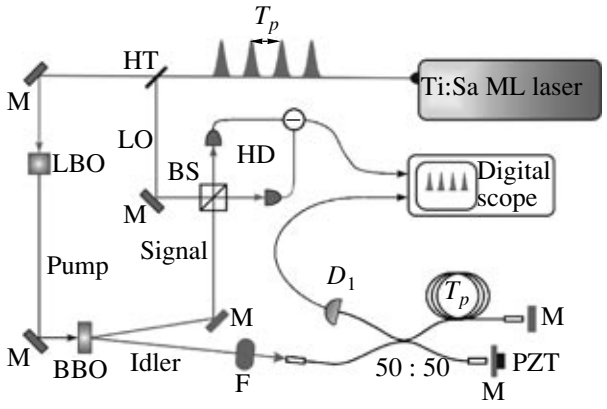

Fig. 1. (Color online) schematic representation of the experimental setup. 50 : 50 is a 3-dB fiber coupler, HT is a high-transmission beam splitter, and M are mirrors. See text for further details.

we present the experimental data obtained by performing two-mode homodyne detection and we describe the reconstruction methods employed to perform two-mode quantum tomography, thus reconstructing both the density matrix and Wigner function of the system under investigation. Furthermore, a detailed comparison with the theoretical predictions is offered. In Section 4, we summarize and discuss our results.

2. TEMPORALLY DELOCALIZED SINGLE PHOTON: EXPERIMENTAL SETUP

The experimental setup is pictured in Fig. 1. The 1.5-ps pulses at 786 nm from a mode-locked Ti:Sapphire laser at a repetition rate of 82 MHz are frequency-doubled in a LBO crystal. The resulting pulse train impinges on a nonlinear BBO crystal cut for degenerate ($\Omega_s = \Omega_i = \Omega_p/2$) noncollinear type-I spontaneous parametric down conversion (SPDC); signal-idler photon pairs centered around 786 nm are thus generated in two distinct spatial modes. A single mode fiber and a pair of etalon interference filters (F) are employed for spatial and spectral filtering of the idler beam before its entrance in a fiber-coupled piezo-controlled (PZT) Michelson interferometer; a single-photon detector (D_1) is inserted at the exit port of the interferometer. The signal beam propagates in free space before being mixed at a 50/50 beam splitter (BS) with a local oscillator (LO) for high-frequency time-domain balanced homodyne detection (HD) [11, 13, 14].

Spatial and spectral filtering of the idler mode are aimed at the conditional projection of the signal photons into a single-photon pure state [15–17]. On the other hand, the role of the Michelson interferometer is to generate indistinguishability between two consecutive time bins propagating in the idler channel: an idler photon detected by D_1 may have been generated by either the nth or the $(n + 1)$th pump pulse, provided that the time delay (T) between the short and long arms of the interferometer is chosen to be approximately equal to the time separation between two consecutive pump pulses (T_p = 12.3 ns). Notice that the bandpass of the spectral filter in the idler arm (σ_i = 50 GHz) is wide enough so that the first-order interference is washed out ($\sigma_i \gg \pi/T_p$).

Based on a standard quantum mechanical calculation [3, 18, 19], we find that, in the setup described above, the combination of indistinguishability and tight filtering in the idler channel allows the conditional remote preparation, in the signal channel, of the temporally delocalized single-photon ebit:

$$|\Psi_s^{\phi_i}\rangle = \frac{1}{\sqrt{2}}(|1^{(n)}, 0^{(n+1)}\rangle + e^{-i\phi_i}|0^{(n)}, 1^{(n+1)}\rangle), \quad (2)$$

with $\phi_i = \Omega_p(T_p - T/2)$. A single photon is thus seen to be coherently delocalized between two consecutive copropagating and nonoverlapping temporal modes or time bins. It is interesting that the relative phase ϕ_i characterizing the remotely prepared ebit is defined not only by the phase difference introduced by the Michelson interferometer ($\varphi_{\text{int}} = \Omega_i T$), but also by the relative phase between consecutive pump pulses ($\varphi_{\text{pump}} = \Omega_p T_p$).

An important advantage of such a remote state preparation scheme is the possibility of changing the relative phase ϕ_i characterizing the signal single-photon state of Eq. (2) by performing simple and reversible operations in the idler arm (or on the train of pump pulses), without performing any manipulation on the signal photons and, hence, without introducing either losses or decoherence.

3. QUANTUM HOMODYNE TOMOGRAPHY

Practical applications of the remotely prepared optical ebit described in Section 2 rely on the existence of a tool for evaluating its degree of purity. In fact, in any realistic situation, the vacuum, multiphoton contributions, and decoherence, as well as imperfect filtering in the idler arm, tend to contaminate the purity of the remotely prepared single-photon state. From this perspective, quantum tomography (i.e., the reconstruction of the density matrix and Wigner function) represents an extremely convenient technique with respect to photon-counting interference-based experiments, which are insensitive to the vacuum contribution. In addition, since we are dealing with a temporally delocalized single photon, we also need a tool to study the correlations characterizing the time bins carrying the delocalized single photon. As we shall see, two-mode homodyne tomography is a very convenient way to achieve this goal.

3.1. Basics of Quantum Homodyne Tomography

The experimental reconstruction of the Wigner function $W(x, y)$ of a given state can be realized by measuring its marginal distributions, namely, $P(X, \theta) = \int_{-\infty}^{+\infty} W(X\cos\theta - Y\sin\theta, X\sin\theta + Y\cos\theta)dY$, for all possible values of θ ranging from 0 to π. The marginal distributions $P(X, \theta)$ can be measured by performing balanced homodyne detection [20]: the state under investigation is spatially and temporally mode-matched to an intense reference local oscillator (LO) coherent field at a 50/50 beam splitter, and the intensities measured by two photodiodes placed at the output ports of the beam splitter are subtracted (see Fig. 1). The rotated field quadratures of the state $|\psi\rangle$ to be analyzed, namely, $X(\theta) = x\cos\theta + y\sin\theta$, are indeed given by $\langle\psi|\hat{X}_\theta|\psi\rangle \propto \int_0^{T_p}(I_1 - I_2)/(2|\alpha|)dt$, where $|\alpha|$ is the amplitude of the local oscillator, θ is the relative phase between signal and local oscillator, and I_j is the intensity measured by the j photodiode ($j = 1, 2$). For each fixed value of the relative phase θ, one can thus obtain the distribution $P(X, \theta)$. Then, from the collection of the measured marginal distributions obtained at different θ, it is possible to reconstruct the Wigner function using quantum homodyne tomography [20, 21].

3.2. Single-Mode Homodyne Tomography

As a preliminary measurement, we performed single-mode quadrature measurements in the signal channel for two different situations: (I) one arm of the remote interferometer is closed and (II) both arms of the remote interferometer are open. In the first case, upon detection of an idler photon, the signal should be projected into a pure single-photon Fock state on a well-defined time bin; hence, this preliminary measurement aims to quantify the overall experimental efficiency of our setup, namely, the preparation and the detection efficiencies. In the second case, upon detection of an idler photon, the signal should be projected into the time-bin entangled single-photon state of Eq. (2); a single-mode measurement in this case aims to better understand the differences between single and two-mode homodyne tomography for systems similar to the one under investigation.

In Fig. 2,we show the reconstructed Wigner function obtained by performing conditional single-mode balanced homodyne detection in the signal channel, when the short arm of the Michelson interferometer is blocked. In this case, there is only one possible path for the idler photon to the trigger detector, so that no ambiguity is left for the time bin occupied by the single signal photon. The Wigner function is calculated using the density matrix elements reconstructed from 5×10^4 quadrature measurements on the selected time bin using the "pattern-function" method developed by D'Ariano et al. [21, 22].

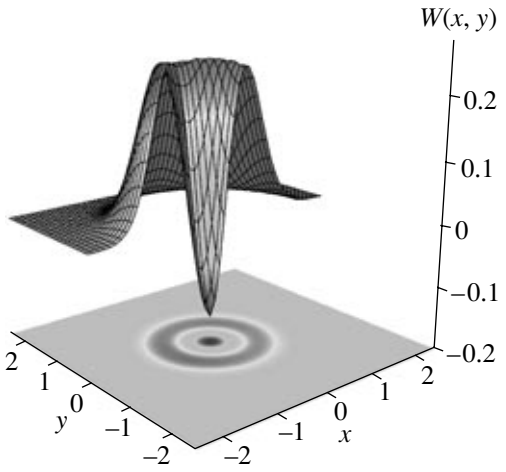

Fig. 2. Single-mode Wigner function obtained by performing homodyne measurements in the signal channel when the short arm of the Michelson interferometer in the idler channel is blocked.

The ideal Wigner function one expects to obtain in this case is the well-known Wigner function for a single-photon Fock stale, namely,

$$W_1(x, y) = \frac{2}{\pi}(4x^2 + 4y^2 - 1)e^{-2(x^2+y^2)}. \quad (3)$$

However, due to nonunitary preparation and detection efficiencies (η_p and η_d, respectively), the measured system is not a pure single-photon Fock state but rather a statistical mixture:

$$\hat{\rho}_1^\eta = (1 - \eta)|0\rangle\langle 0| + \eta|1\rangle\langle 1|, \quad (4)$$

where $\eta = \eta_p\eta_d$ is the overall experimental efficiency. In this case, losses due to both the impurity of the prepared single-photon state and the imperfect detection efficiency (mode matching and quantum efficiency of the photodiodes) can be modeled by a beam splitter with transmittance η placed before an ideal homodyne detector. As shown in [20], the realistic Wigner function is given by the convolution between the Wigner function of a single-photon Fock state $W_1(x, y)$ and the Wigner function of the vacuum $W_0(x, y) = 2/\pi e^{-2(x^2+y^2)}$, both scaled by a factor depending on the overall efficiency η:

$$W_1^\eta(x, y) = (1 - \eta)W_0(x, y) + \eta W_1(x, y). \quad (5)$$

This result indicates that an important advantage of reconstructing the Wigner function and, more generally, of performing quantum tomography is the possibility of obtaining information about the losses affecting the system under investigation and, hence, about the vacuum contamination.

Comparison of the experimentally reconstructed Wigner function (Fig. 2) with the realistic theoretical prediction of Eq. (5) indicates that our setup is characterized by an overall efficiency of $\eta = 0.61$. Hence, the

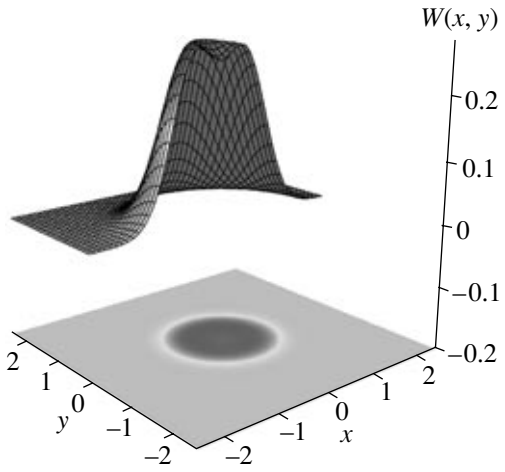

Fig. 3. Reconstructed Wigner function corresponding to single-mode homodyne measurements performed in the signal channel when both arms of the remote interferometer, in the idler channel, are open. The detected system is a statistical mixture composed of $(1 - \eta/2) = 69.5\%$ vacuum and $\eta/2 = 30.5\%$ of single-photon Fock state.

single-photon Fock state we wished to produce is contaminated, after measurement, by 39% of vacuum.

Let us now consider our second data set. In Fig. 3, we show the reconstructed Wigner function obtained by performing conditional single-mode homodyne detection in the signal beam, when both arms of the remote interferometer are open. Now, since both possible paths are allowed for the idler photon to reach the trigger detector, there is no information as to which time bin is occupied by the signal photon, and a single-mode measurement will detect it only half of the time. As before, the density matrix has been reconstructed directly from the experimental data (i.e., 10^6 phase-independent quadrature measurements).

In this second case, we expect the conditionally prepared system to be described by the delocalized single-photon state of Eq. (2), which involves two time bins. However, since our single-mode measurements only involve one time bin, the detected system is not described by Eq. (2) but is rather given, even in the ideal case, by the statistical mixture

$$\hat{\rho}_{\rm mix} = \frac{1}{2}(|0\rangle\langle 0| + |1\rangle\langle 1|), \qquad (6)$$

as can easily be seen by taking the partial trace of the density matrix corresponding to Eq. (2) over the undetected time bin. The ideal Wigner function is now given by $W_{\rm mix}(x, y) = [W_0(x, y) + W_1(x, y)]/2$. Hence, after accounting for the losses, we expect the reconstructed Wigner function to be described by

$$W^{\eta}_{\rm mix}(x, y) = \left(1 - \frac{\eta}{2}\right)W_0(x, y) + \left(\frac{\eta}{2}\right)W_1(x, y), \qquad (7)$$

with η equal to the value experimentally obtained from the previous measurement. In other words, we expect the single-mode Wigner function to be the same we found in the single-arm case, but with half the efficiency.

The experimentally reconstructed Wigner function of Fig. 3 is in very good agreement with this theoretical prediction (Eq. (7)). Both the experimental results and the discussion carried above explicitly show the necessity of performing two-mode homodyne detection: the single-mode analysis does not suffice to completely characterize the remotely prepared system; for instance, it is unable to reproduce the correlations that may exist between consecutive time bins.

3.3. Two-Mode Homodyne Tomography

Two-mode homodyne tomography has been used to reconstruct the complete quantum state of the prepared two-mode state of Eq. (2). In this case, the reconstruction of both the density matrix and two-mode Wigner function requires measuring the joint marginal distributions of the quadratures $X_1(\theta_1) = x_1\cos\theta_1 - y_1\sin\theta_1$ and $X_2(\theta_2) = x_2\cos\theta_2 - y_2\sin\theta_2$ for different values of the phases θ_1 and θ_2 of two LO pulses spatially and temporally matched (i.e., synchronized) to temporal modes 1 and 2, respectively. However, since the particular state investigated here comes from a single-photon Fock state, it is expected to be invariant with respect to the global phase; hence, only the relative phase $\Delta\theta = \theta_1 - \theta_2$ needs to be controlled in the experiment [20, 23]. In addition, for the state of Eq. (2), the joint marginal distribution $P(X_1, X_2, \Delta\theta)$ is invariant under interchange of ϕ_i and $\Delta\theta$. We exploited this property to overcome the difficulty connected to the generation of a pair of phase-controllable LO pulses out of the train coming from the laser. Rather than varying the relative LO phase, one may use any two consecutive pulses directly from the mode-locked train and remotely vary the phase ϕ_i by means of the interferometer in the idler channel. Although what we actually do in this case is to measure fixed quadratures on the two modes for a varying quantum state $|\Psi_s^{\phi_i}\rangle$, it is immediate to show that this is equivalent to performing a conventional LO phase scan of the fixed quantum state $|\Psi_s^{\phi_i = \rm const}\rangle$. We shall call this technique "remote balanced homodyne tomography."

While keeping both the local oscillator and the homodyne detection apparatus unchanged, we have thus performed stable and fast quadrature measurements for different values of the interferometer delay T (and hence of ϕ_i). Upon detection of each idler photon, a fast-sampling digital scope acquires the homodyne signal of the two corresponding signal time bins (plus one containing just the vacuum, which is used for calibration); the quadrature value for each time bin is then extracted as proportional to the integral of the homo-

dyne signal over the corresponding time interval. A total of 10^6 quadrature measurements, equally distributed over the range $[0, \pi]$ of ϕ_i, was performed following this procedure on each of the three time bins.

The experimental results are shown in Fig. 4, where we plot the measured values of the quadratures X_1 and X_2 obtained for three different values of the remotely varied phase ϕ_i while leaving unchanged the relative phase between LO pulses. According to the above reasoning, these results also represent the marginal distributions $P(X_1, X_2, \Delta\theta)$ associated with the ebit of Eq. (2) for $\phi_i = 0$ and obtained for three different values of the relative phase $\Delta\theta$. Notice that, while the joint distribution $P(X_1, X_2, \Delta\theta)$ is strongly phase-dependent, the marginal distributions $P(X_1)$ and $P(X_2)$ associated with each time bin, separately, are phase-independent. This is consistent with the fact that each mode, separately, is an incoherent statistical mixture of the vacuum and a single-photon Fock state, as indicated by Eq. (6). However, the two-mode measurements reproduce the correlations characterizing the pair of time bins 1 and 2 as a whole, thus revealing the existence of a coherent superposition, as expected from Eq. (2). Figure 4 also shows that a single-photon Fock state exists in the "center of mass" phase space defined by the coupled quadratures $(x_1 + x_2, y_1 + y_2)$, while vacuum is found in the phase space $(x_1 - x_2, y_1 - y_2)$. In fact, the marginal distribution $P(x_1 + x_2)$ reported above Fig. 4c is fitted very well by the marginal distribution associated with a single-photon Fock state when the overall experimental efficiency is $\eta = 0.61$. This is perfectly in line with the result we found in the first measurement set described in Section 3.2, when one arm of the remote interferometer was kept closed.

The homodyne data have been directly employed to reconstruct the two-mode density matrix, following the "pattern functions" method [20, 22]. The two-mode density matrix element $\rho_{klmn} = \langle k, l|\hat{\rho}|m, n\rangle$ is given by the statistical average of the corresponding pattern functions over the homodyne data, which is written as

$$\rho_{klmn} = \langle f_{km}(X_1, \theta_1) f_{ln}(X_2, \theta_2)\rangle, \quad (8)$$

where the function average is taken over the experimental values of the quadratures X_1 and X_2 measured on the two modes at the fixed phases θ_1 and θ_2, respectively. By rewriting the pattern functions as $f_{mn}(x, \theta) = F_{mn}(x)e^{-i(n-m)\theta}$, the above expression can be simplified to give

$$\rho_{klmn} = \langle F_{km}(X_1) F_{ln}(X_2) e^{-i[(m-k)\theta_1 + (n-l)\theta_2]}\rangle, \quad (9)$$

where $F_{mn}(x)$ are given in [20, 21]. Thus, when the state under investigation only depends on the phase difference $\Delta\theta = \theta_2 - \theta_1$, the nonzero terms are those elements having $k - m = -(l - n)$.

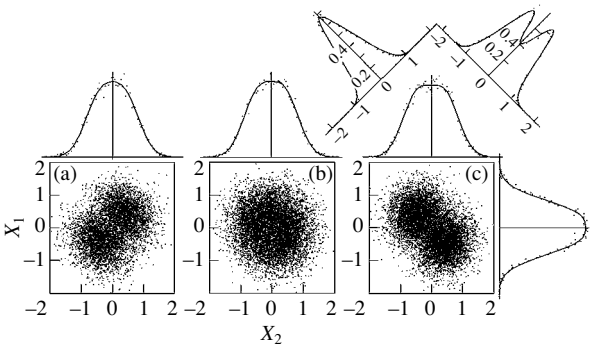

Fig. 4. Joint marginal distributions of the field quadratures measured on two modes for: (a) $\phi_i = 0$, (b) $\pi/2$, (c) π, while leaving the LO unchanged. These are also the joint marginal distributions $P(X_1, X_2, \Delta\theta)$ associated with the ebit of Eq. (2) for $\phi_i = 0$, and corresponding, respectively, to $\Delta\theta = 0, \pi/2, \pi$. The histograms are the single-mode marginal distributions $P(X_1)$ and $P(X_2)$ together with the corresponding best fits. The marginal distributions for the coupled quadratures are plotted on the diagonal axes above (c).

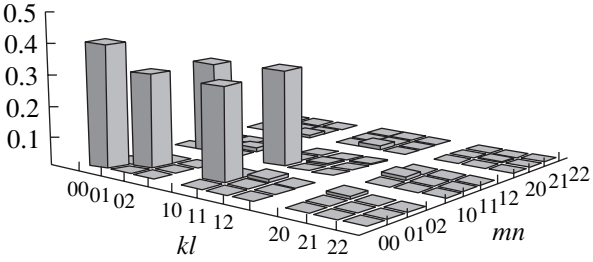

Fig. 5. (Color online) Reconstructed elements of the two-mode density matrix ($\rho_{klmn} = \langle k_1 l_2|\hat{\rho}|m_1 n_2\rangle$).

Figure 5 shows the reconstructed density matrix, which can be expressed as $\hat{\rho} = (1 - \eta)|0\rangle\langle 0| + \eta|\Psi_s^{\phi_i = 0}\rangle\langle\Psi_s^{\phi_i = 0}|$. Notice indeed that almost no multiphoton contribution exists. The overall efficiency $\eta = 0.605$, evaluated from the vacuum component, is essentially the same we found in Section 3.2. From Fig. 5, it is also apparent that the vacuum contamination and hence the losses do not degrade the coherence of the remotely delocalized single photon; in fact, both the nondiagonal and the diagonal ($|01\rangle\langle 01|$ and $|10\rangle\langle 10|$) elements of the reconstructed density matrix are reduced by the same amount. This may be understood as a consequence of the common losses undergone by the pair of entangled time bins.

Finally, the density matrix elements were used to reconstruct the Wigner function [11, 12, 20, 21]:

$$W(x_1, y_1; x_2, y_2) = \sum_{k,l,m,n} \rho_{klmn} W_{km}(x_1, y_1) W_{ln}(x_2, y_2), \quad (10)$$

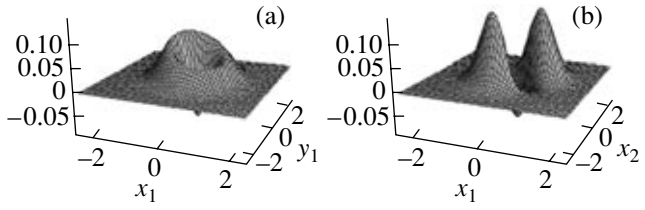

Fig. 6. (Color online) Cross sections of the reconstructed two-mode Wigner function: (a) $W^{\phi_i = 0}(x_1, y_1; -0.1, -0.1)$, and (b) $W^{\phi_i = 0}(x_1, 0; x_2, 0)$.

where $W_{mn}(x, y)$ is the Wigner function associated with the projector $|m\rangle\langle n|$, which is given by

$$W_{mn}(x, y) = \frac{2}{\pi}\int d\xi \langle x + \xi|m\rangle\langle n|x - \xi\rangle e^{-4iy\xi}. \quad (11)$$

Figures 6a and 6b reproduce, respectively, the (x_1, y_1) and (x_1, x_2) sections of the reconstructed 4D Wigner function $W^{\phi_i = 0}(x_1, y_1; x_2, y_2)$. The cross section (x_1, y_1) resembles the standard Wigner function of a single-photon Fock state but is characterized by a well-defined phase. The (x_1, x_2) section of the reconstructed two-mode Wigner function explicitly shows the correlation between the quadratures x_1 and x_2; the nonfactorable nature of the delocalized single photon is apparent here. The observation of both the phase dependence of the Wigner function and the correlations between field quadratures associated with two separate time bins are the result of the ability of our balanced homedyne detector to resolve two consecutive temporal modes, thus performing separate measurements over each time bin carrying the delocalized single photon.

The results of Fig. 6 are in agreement with the expected two-mode Wigner function corresponding to the delocalized single photon of Eq. (2). In fact, the ideal theoretical Wigner function is given by

$$W^{\phi_i}(x_1, y_1; x_2, y_2) = \frac{1}{2}[8W_{10}^{\phi_i}(x_1, y_1; x_2, y_2) + W_1(x_1, y_1)W_0(x_2, y_2) + W_0(x_1, y_1)W_1(x_2, y_2)], \quad (12)$$

where W_1 and W_0 are the single-photon and the vacuum Wigner functions, respectively, as given in Section 3.2; $W_{10}^{\phi_i}(x_1, y_1; x_2, y_2)$, on the other hand, is a nonfactorable 4D function which couples the quadratures of two consecutive nonoverlapping signal time bins:

$$W_{10}^{\phi_i}(x_1, y_1; x_2, y_2) = W_0(x_1, y_1)W_0(x_2, y_2)(x_1 x_2^{\phi_i} + y_1 y_2^{\phi_i}), \quad (13)$$

where $x_2^{\phi_i} = x_2\cos\phi_i - y_2\sin\phi_i$ and $y_2^{\phi_i} = x_2\sin\phi_i + y_2\cos\phi_i$. Hence, the Wigner function associated with the delocalized signal photon is expected to contain information about the characteristic phase ϕ_i introduced through the idler arm and, in particular, to reproduce the correlations remotely generated between pairs of well-separated time bins in the signal arm.

The results of Eqs. (12) and (13) explicitly indicate that the delocalized single photon cannot be studied in terms of the quadratures associated with neither one of the two distinct time bins 1 and 2, separately; the modes associated with the two time bins carrying the delocalized single photon need to be analyzed together.

The agreement between the above theoretical prediction and the experimental results of Fig. 6 becomes evident when accounting for the experimental efficiency. In this case, by extending to two modes the procedure employed to obtain Eq. (15), we get:

$$W_\eta^{\phi_i}(x_1, y_1; x_2, y_2) = (1 - \eta)W_0(x_1, y_1)W_0(x_2, y_2) + \eta W^{\phi_i}(x_1, y_1; x_2, y_2). \quad (14)$$

Both this result and Fig. 6 indicate that losses essentially affect the negativity of the two-mode Wigner function; however, both the correlation between quadratures associated with two distinct time bins and the phase information are mostly left unchanged by the vacuum contamination.

In summary, the experimental reconstruction of the two-mode Wigner function of a conditionally prepared single-photon ebit has enabled us to verify its entangled nature and study its purity. The reconstructed two-mode Wigner function has indeed been found to reproduce both the fixed relative phase and the consequent correlation existing between time bins 1 and 2, as expected from Eq. (12).

4. CONCLUSIONS

In conclusion, we have demonstrated the application of a novel dual-temporal-mode ultrafast homodyne detection technique for the tomographic analysis of quantum light states. This scheme has proved its capability of working at the full repetition rate of the mode-locked laser source (82 MHz) and to be able to accurately operate on distinct picosecond time bins separated by just a few nanoseconds. Although it has been demonstrated here for the relatively simple case of only two successive time-bins, the scheme is immediately expandable to higher dimensionality and to more complex temporal sequences, thus allowing for any kind of time-bin entanglement to be fully characterized.

Our novel detection scheme is also useful from the viewpoint of fundamental physics: other than studying the entanglement as we have done here, recent developments indicate the possibility of employing quantum homodyne tomography for testing quantum nonlocality by the violation of Bell's inequality [24, 25]. The tomographic approach might benefit from the higher efficiencies characteristic of homodyne detection to

achieve the first loophole-free proof of quantum nonlocality.

5. ACKNOWLEDGMENTS

This work was performed in the framework of the "Spettroscopia laser e ottica quantistica" project of the Department of Physics of the University of Florence and was supported in part by Ente Cassa di Risparmio di Firenze and MIUR under the PRIN initiative and FIRB contract RBNE01KZ94.

REFERENCES

1. S. Giacomini, F. Sciarrino, E. Lombardi, and F. De Martini, Phys. Rev. A **66**, 030302 (2002).
2. E. Knill, R. Laflamme, and G. J. Milburn, Nature (London) **409**, 46 (2001).
3. J. Brendel, N. Gisin, W. Tittel, and H. Zbinden, Phys. Rev. Lett. **82**, 2594 (1999); H. de Riedmatten, I. Marcikic, V. Scarani, et al., Phys. Rev. A **69**, 050304 (2004).
4. J. D. Franson, Phys. Rev. Lett. **62**, 2205 (1989).
5. C. Simon, and J.-P. Poizat, Phys. Rev. Lett. **94**, 030502 (2005).
6. A. Zavatta, M. D'Angelo, V. Parigi and M. Bellini, Phys. Rev. Lett. **96**, 020502 (2006).
7. H. de Riedmatten, I. Marcikic, W. Tittel, et al., Phys. Rev. Lett. **92**, 047904 (2004).
8. T. B. Pittman, B. C. Jacobs, and J. D. Franson, Phys. Rev. A **71**, 032307 (2005).
9. W. Tittel, J. Brendel, H. Zbinden, and N. Gisin, Phys. Rev. Lett. **84**, 4737 (2000).
10. I. L. Chuang and Y. Yamamoto, Phys. Rev. Lett. **76**, 4281 (1996).
11. A. Zavatta, S. Viciani, and M. Bellini, Phys. Rev. A **70**, 053821 (2004).
12. A. Zavatta, S. Viciani, and M. Bellini, Science **306**, 660 (2004); Phys. Rev. A **72**, 023820 (2005).
13. A. Zavatta, S. Viciani, and M. Bellini, Laser Phys. Lett. **3**, 3 (2006).
14. A. Zavatta, M. Bellini, P. L. Ramazza, et al., J. Opt. Soc. Am. B **19**, 1189 (2002).
15. T. Aichele, A.I. Lvovsky, and S. Schiller, Eur. Phys. J. D **18**, 237 (2002).
16. M. Bellini, F. Marin, S. Viciani, et al., Phys. Rev. Lett. **90**, 043602 (2003).
17. S. Viciani, A. Zavatta, and M. Bellini, Phys. Rev. A **69**, 053801 (2004).
18. D. N. Klyshko, *Photon and Nonlinear Optics* (Gordon and Breach Sci., New York, 1988).
19. T. E. Keller, and M. H. Rubin, Phys. Rev. A **56**, 1534 (1997); Y.-H. Kim, V. Berardi, M. V. Chekhova, et al., Phys. Rev. A **62**, 043820 (2000).
20. U. Leonhardt, *Measuring the Quantum State of Light* (Cambridge Univ. Press, Cambridge, 1997).
21. G. M. D'Ariano, in *Quantum Optics and Spectroscopy of Solids*, Ed. by T. Hakioglu and A. Shumovsky (Kluwer Academic, Dordrecht, 1997), pp. 175–202.
22. G. M. D'Ariano, C. Macchiavello, and M. G. A. Paris, Phys. Rev. A **50**, 4298 (1994).
23. S. A. Babichev, J. Appel, and A. I. Lvovsky, Phys. Rev. Lett. **92**, 193601 (2004).
24. K. Banaszek and K. Wodkiewicz, Phys. Rev. Lett. **82**, 2009 (1999).
25. M. D'Angelo, A. Zavatta, V. Parigi and M. Bellini, (2006) (submitted); quant-ph/0602150.